Research Article | Vol. 31, No. 23 / 6 Nov 2023 / Optics Express 39279
Optics EXPRESS

Dark field imaging of high aspect ratio structures – a simple model

RICHARD R. A. SYMS,* FU YEE KWAN, AND OLEKSIY SYDORUK

EEE Dept., Imperial College London, Exhibition Road, London SW7 2BX, UK
*r.syms@imperial.ac.uk

Abstract: A simplified model for dark-field optical imaging of three-dimensional high aspect ratio micro- and nano- structures is proposed, to reduce the time taken to simulate object fields with in-plane scattering between different parts of the object. Primary scattering is found by assuming that illumination of Manhattan geometries generates a set of spherical edge waves, following the incremental theory of diffraction. Secondary scattering is found by assuming that primary scattering is re-scattered from nearby features. Diffraction coefficients are simplified, and the number of illuminating beams is limited to those generating waves that enter the objective lens. Images obtained using TE and TM polarizations are compared, and results are benchmarked against a vectorial finite element model. Applications lie in simulating optical inspection of structures containing vertically etched features including MEMS and NEMS.

Published by Optica Publishing Group under the terms of the Creative Commons Attribution 4.0 License. Further distribution of this work must maintain attribution to the author(s) and the published article's title, journal citation, and DOI.

1. Introduction

Modelling of optical microscopy is long established [1]. The initial task is computation of the object field, but for simplicity multiple scattering was ignored to begin with [2,3] and the objective lens was then described in terms of an aplanatic factor and a pupil function [4]. Interest was renewed by the need to model inspection of very-large-scale integrated (VLSI) circuits, but multiple scattering could no longer be ignored for closely spaced relief structures such as photoresist patterns. To simplify the problem, two-dimensional (2D) periodic structures were often assumed [5–8], allowing the use of modal theory [9,10] or rigorous coupled-wave analysis (RCWA) [11,12] to simulate scattered fields. More recently, imaging of 3D structures has been modelled using RCWA [13,14], finite element modelling (FEM) [15,16], RCWA and FEM [17,18], finite difference time domain (FDTD) [19–21], vector potential [22], and integral equation [23] methods. However, the computation to model multiple polarizations, incidence angles and wavelengths is extensive [19] and has involved supercomputers [20].

An alternative method of modelling scattering from isolated structures is the geometrical theory of diffraction (GTD), which approximates exact solutions for infinitely long conducting knife edges and wedges [24] as a sum of transmitted, reflected, and diffracted waves [25]. Diffraction coefficients have been refined to improve matching at near-field boundaries in the physical [26] and uniform [27] theories of diffraction (PTD and UTD). The different theories have been compared [28], and diffraction coefficients have been found for other canonical objects such as slits and apertures [29,30]. Arrangements of multiple objects have been tackled by using ray tracing to compute the result of multiple scattering [31–34], and finite and curved edges have been modelled using a local diffraction coefficient in the incremental theory of diffraction (ITD) [35–38]. GTD has been used in projection lithography simulations, accounting for both edge and vertex diffraction [39,40]. However, computations are again lengthy.

Here we consider a further problem for which a general simulation method is required, namely optical imaging of high aspect ratio (HAR) structures. Applications include inspection of masks and nanoimprint templates [41,42], vias and low-density microelectronics [43,44],

#504830 https://doi.org/10.1364/OE.504830
Journal © 2023 Received 31 Aug 2023; revised 26 Oct 2023; accepted 26 Oct 2023; published 3 Nov 2023

Optics EXPRESS

microelectromechanical systems (MEMS) [45], and nanostructures [46]. For MEMS, optical microscopy is often used to avoid slow, expensive, and potentially damaging electron beam inspection of suspended structures. In bright field, nanoscale features appear as dark lines, and microscale features as dark edges [47]. In dark field (DF), background from the substrate and superstrate is eliminated, and the entire image is composed of bright edge waves. Scattering from nanoscale parts is increased, and this difference has been exploited to segment images based on brightness curvature [48]. In each case, device appearance is heavily modified, and simulated images are required to allow defect identification. We propose an approximate model of DF imaging of HAR structures based on layout segmentation, ITD, and Fourier analysis.

Figure 1 shows the main assumptions. Structures (cyan, Fig. 1(a)) are simplified by assuming Manhattan geometries, so that edges can be found by Sobel filtering. Primary scattering is modelled by assuming that edges generate spherical waves (green, Fig. 1(b)), and secondary scattering is estimated by re-scattering of in-plane radiation. Imaging is simulated by assuming that only edge waves are collected by the objective lens, which has an acceptance cone with half-angle θ_L (violet, Fig. 1(a)) and acts as a low-pass spatial filter. The model is further simplified by approximating diffraction coefficients and reducing the number of illuminating wave angles (θ_0, ψ_0) to those contributing most to the image, the four waves at normal incidence to each edge type shown by arrows in Fig. 1(a).

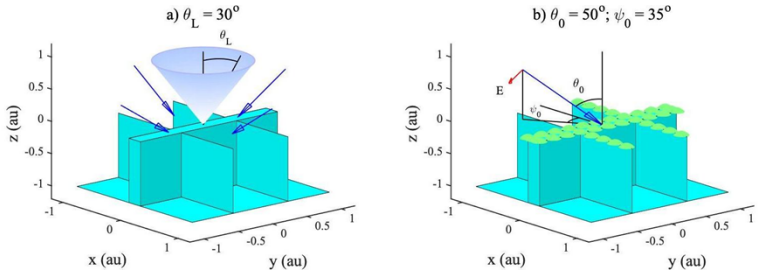


Fig. 1. a) Geometry for DF imaging; b) scattering of spherical waves from edges.

The arrangement of the paper is as follows. Section 2 develops an approximate scattering model for TE and TM dark-field imaging of a restricted set of two-dimensional (2D) structures, and Section 3 compares simulated 1D images with the predictions of FEM. Section 4 extends the model to arbitrary 3D structures, and Section 5 compares simulated 2D images with FEM. Despite the sweeping simplifications, the model predictions are surprisingly accurate for layouts with moderate feature separation, and the computation needed to simulate imaging of complex device layouts is significantly reduced compared with FEM. Section 6 draws conclusions and discusses how the model may be extended.

2. Approximate 2D scattering model

A 2D simulation model for dark-field microscopy of HAR MEMS may be developed by making simplifying assumptions concerning the objects, illumination, scattering, and imaging. For example, silicon has moderate conductivity, for which a perfect electric conductor (PEC) provides a reasonable approximation and GTD coefficients are well known. The use of deep reactive ion etching leads to large feature depths, so the substrate may be ignored as being out-of-focus. Devices often consist of mesas or suspended parts in Manhattan geometries. Upper surfaces are largely planar, so that only a single device layer need be considered, and so on.

These assumptions allow scattering models to be based on rigorous diffraction theories. For example, Fig. 2(a) shows diffraction from a right-angled PEC wedge, which is representative of a

Optics EXPRESS

HAR mesa edge (see e.g. [28]). Here a plane wave is incident at an angle ϕ_0 and wavelength λ in the leading direction. According to GTD, solutions to the electromagnetic problem may be decomposed into the sum of incident and diffracted waves in Region I, and incident, reflected and diffracted waves in Regions II and III. In Fig. 2(b), illumination is in the trailing direction, and Region III now contains incident, reflected and diffracted waves, Region I incident and diffracted waves, and Region II diffracted waves alone. In each case, an objective lens with an acceptance cone of half-angle θ_L will collect light only from within this range. In dark field imaging, when all illuminating waves lie outside the acceptance cone, no reflected waves can enter the lens, and only the diffracted edge waves are important. We now consider them further.

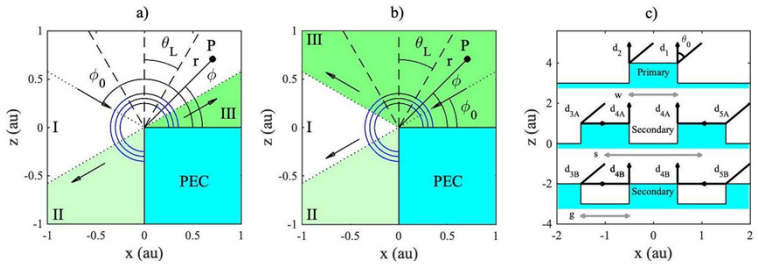


Fig. 2. 2D model of scattering from a right-angle wedge with a) leading and b) trailing edge illumination. c) scattering from general stepped profiles.

At a far-field point $P(r, \phi)$, the edge waves are cylindrical, and can be written as [25]:

$$A_E = E_I D \frac{\exp(-jk_0 r)}{\sqrt{r}} \tag{1}$$

Here r is radial distance, $k_0 = 2\pi/\lambda$, E_I is the illuminating wave amplitude and D is the diffraction coefficient. The coefficient varies with ϕ_0, ϕ and polarization, and is different in GTD, PTD and UTD. However, any differences are largely unimportant away from the boundaries between regions. In GTD, for example, the diffraction coefficient for a wedge is:

$$D(\phi, \phi_0) = \frac{\exp\left(-j\frac{\pi}{4}\right)}{\sqrt{2\pi k_0}} d(\phi, \phi_0) \tag{2}$$

Here the angular dependency is specified by the reduced coefficient d:

$$d = \frac{\sin\left(\frac{\pi}{n}\right)}{n} \left\{ \frac{1}{\cos\left(\frac{\pi}{n}\right) - \cos\left(\frac{\phi-\phi_0}{n}\right)} \pm \frac{1}{\cos\left(\frac{\pi}{n}\right) - \cos\left(\frac{\phi+\phi_0}{n}\right)} \right\} \tag{3}$$

Here n is a constant (for right-angle wedge, $n = 3/2$), and negative and positive signs are for TE and TM polarization, respectively. Diffraction coefficients may be used in scattering models of more complex structures. For example, Fig. 2(c) shows a plane wave incident at $\theta_0 = 90^o - \phi_0$ on general HAR surfaces, which present leading and trailing edges simultaneously. Primary scattering in the vertical direction is described by the reduced coefficients d_1 and d_2 with $\phi = 90^o$. If their variation over the acceptance cone is limited, these terms may be taken as constant for a given ϕ_0. Secondary scattering may take place across mesa plateaus and air gaps and is described by coefficients d_{3A}, d_{4A}, d_{5A} and d_{3B}, d_{4B}, d_{5B}, found from Eqn. (3) with the relevant values of ϕ and ϕ_0. For $\theta_0 = 50^o$, for example, the values in Table 1 are obtained.

Additional ratios R_1, R_{2A}, R_{3A}, R_{2B} and R_{3B} can be calculated as shown in Table 1 and help understand the relative significance of scattering processes. Their values imply that TE primary

Optics EXPRESS

Table 1. TE and TM diffraction coefficients and scattering ratios for $\theta_0 = 50°$.

	d_1	d_2	d_{3A}	d_{4A}	d_{5A}	d_{3B}	d_{4B}	d_{4B}
TE	-1.899	+0.602	0	0	0	−2.135	−1.732	−3.028
TM	+1.034	−1.467	−0.829	−1.155	−2.613	+1.307	+0.577	+0.414
	$R_1 = d_2/d_1$	$R_{2A} = d_{3A}d_{4A}/d_1$		$R_{3A} = d_{5A}d_{4A}/d_1$	$R_{2B} = d_{3B}d_{4B}/d_1$		$R_{3B} = d_{5B}d_{4B}/d_1$	
TE	−0.317	0		0	−1.948		−2.761	
TM	−1.418	+0.925		+2.917	+0.729		+0.231	

scattering is larger than TM primary scattering, that TE leading edge diffraction is larger than trailing edge diffraction, and that TE secondary scattering is negligible over mesa plateaus.

These observations allow construction of an imaging model for more complex profiles. The surface is modelled by a general stepped variation in the $x-$ direction, and the incident wave by the illumination function of a plane wave, namely $E_I = E_0\exp\{+jk_0x\sin(\theta_0)\}$. Scattering is simulated by assuming that each edge generates a cylindrical wave whose amplitude is weighted by the illumination at its point of origin and the relevant diffraction coefficient. For example, for TE incidence on a mesa of width w centred on $x = 0$ (Fig. 2(c), upper) there are only two terms, because the coefficients d_{3A}, d_{4A}, d_{5A} are all zero. The scattered electric field may then be approximated as:

$$E(x) = d_1E_I\left(\frac{w}{2}\right)\delta\left(x - \frac{w}{2}\right) + d_2E_I\left(-\frac{w}{2}\right)\delta\left(x + \frac{w}{2}\right) \tag{4}$$

Here $\delta(x)$ is a delta function. The effect of illumination is therefore to modify the scattering from each edge by the amplitude E_I, while the diffraction coefficient provides additional weighting that depends on whether the edge is leading or trailing.

Formation of a unity magnification image is modelled by the normal route of Fourier transformation, multiplication by the aplanatic factor and pupil function, and inverse transformation. For small ray angles θ, the aplanatic factor $F(\theta) = \cos^{1/2}(\theta)$ may be approximated as unity. In the spatial frequency domain, the pupil function P is:

$$P(k_x) = 1, k_x \le k_L; P(k_x) = 0, k_x > k_L \tag{5}$$

Here $k_L = k_0NA$ is the spatial frequency cutoff and $NA = \sqrt{1 - \cos^2(\theta_L)}$ is the numerical aperture. With this approximation, the electric field of the line image may be written as:

$$E_{im}(x) = E_0^{'}\left\{d_1E_I\left(\frac{w}{2}\right)\mathrm{sinc}\left\{k_L\left(x - \frac{w}{2}\right)\right\} + d_2E_I\left(-\frac{w}{2}\right)\mathrm{sinc}\left\{k_L\left(x + \frac{w}{2}\right)\right\}\right\} \tag{6}$$

Here $E_0^{'}$ is a constant, and image inversion has been omitted to aid interpretation. The effect of the pupil function is to broaden each edge in the object into a sinc function, whose amplitude and width depend on k_L. For lenses with low numerical aperture, the linewidth will be broad, but with sufficient illumination an image will be seen even for nanostructures. If w is very small, the image will be approximately a single sinc function; as w increases, two separate lines will appear. These have different amplitudes determined by d_1 and d_2 and sum coherently, with the result depending weakly on the incidence angle θ_0.

For a centered trench of gap g, there are extra terms, because the coefficients d_{3B}, d_{4B}, d_{5B} are non-zero for both polarizations. Using Eqn. (1), and following the paths in Fig. 2(c), we obtain:

$$\begin{aligned} E(x) = &\left\{d_2E_I\left(\tfrac{g}{2}\right) + d_{3B}d_{4B}\tfrac{\exp(-jk_0g)}{\sqrt{g+r_0}}E_I\left(-\tfrac{g}{2}\right)\right\}\delta\left(x - \tfrac{g}{2}\right) + \\ &\left\{d_1E_I\left(-\tfrac{g}{2}\right) + d_{5B}d_{4B}\tfrac{\exp(-jk_0g)}{\sqrt{g+r_0}}E_I\left(\tfrac{g}{2}\right)\right\}\delta\left(x + \tfrac{g}{2}\right) \end{aligned} \tag{7}$$

Here a constant r_0 has been introduced into the secondary diffraction terms to avoid singularities as $g \to 0$. This has no physical meaning but reflects the fact that GTD is a far-field theory and

Optics EXPRESS

the geometry here is near field. Agreement with FEM deteriorates for narrow or wide features as r_0 is reduced or increased, respectively. We have used the empirical value $r_0 = \lambda/2$ for both polarizations, in 2D and later 3D models. Inverse transformation again converts each delta function into a sinc function in the image. Here, the amplitude variation will again contain two lines; however, their amplitudes must differ from those for a mesa. Amplitude images of more complex structures may be constructed similarly. In all cases, the image will contain the same number of lines as edges, and the amplitudes and phases of sinc-function terms will be determined by the scattering. Intensity images may be found from the modulus square of electric fields, and the effects of diffuse, polychromatic illumination may be simulated by summing intensities for TE and TM polarization and incidence at different θ_0 and λ. These additions will modify image details. We now consider the accuracy of these models.

3. 2D numerical results

Results from the scattering model were benchmarked against 3D vectorial FEM simulations using COMSOL Multiphysics. Calculations were performed for PEC mesas of depth $d = 1\mu m$ surrounded by air, omitting any substrate. To reduce computational demands, the domain was restricted to a volume $8\mu m \times 8\mu m \times 2\mu m$. Perfectly matched layers (PMLs) were used at the upper and lower boundaries to avoid reflections at these surfaces, and a Floquet condition was assumed at other boundaries to account for periodicity. An excitation port for an incident plane wave was assigned between the upper PML and the structure. Unity magnification imaging was simulated by Fourier transforming periodic backscatter on the mesa plane to obtain a set of diffraction orders, eliminating orders lying outside the acceptance cone, applying the aplanatic correction, and recombining the orders. Image inversion was again omitted.

Figure 3 compares simulated variations of electric field modulus for mesas of different widths w, assuming single-sided incidence at $\theta_0 = 50^o$ and $\lambda = 0.5\mu m$, a lens with $\theta_L = 30^o$. The upper plots show TE results, the lower TM; these clearly differ in which edge is dominant. The blue and red lines show FEM results and the predictions of the scattering model, respectively; the mesa is sketched in green. As expected, each edge gives rise to a peak in field, but the variations are asymmetric. As w reduces, the peaks approach each other, and eventually merge. In this regime, primary scattering is dominant, and the phase variation imposed by illumination controls the coherent addition of the scattering from the edges. However, the overall patterns and detailed sidelobe structures are both very similar.

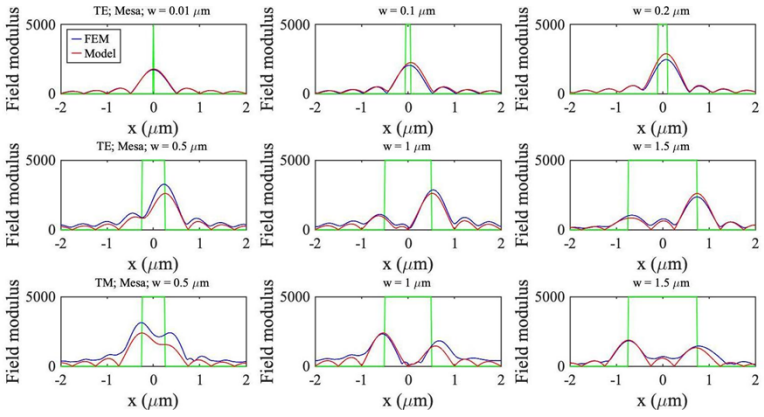


Fig. 3. Line variations of field modulus in images of mesas, for one wave incident at $\theta_0 = 50^o$. Upper – TE, lower – TM. Blue – FEM; red – GTD scattering model; green - structure.

Optics EXPRESS

Figure 4 compares similar variations of electric field modulus for trenches of different gaps g. The upper plots now show TM results, and the lower TE; there are now larger differences in dominant edge between the two polarizations. The blue lines again show FEM results, the red lines show predictions of the scattering model, and the trench is in green. For large gaps, each edge again gives rise to peak in field. However, the images of trenches are not the same as those of mesas: the positions of the peaks often suggest that trenches are narrower than their nominal width, while mesas appear wider. This difference is due to secondary scattering. At moderate widths, the scattering model performs well, but its ability to model short range effects is limited. There is again in-plane resonance, but agreement is now only acceptable for g>0.5 μm. For some widths (g = 0.01 μm and g = 0.5 μm), disagreement between the models can be large, implying that higher order terms omitted from the scattering model must also be significant.

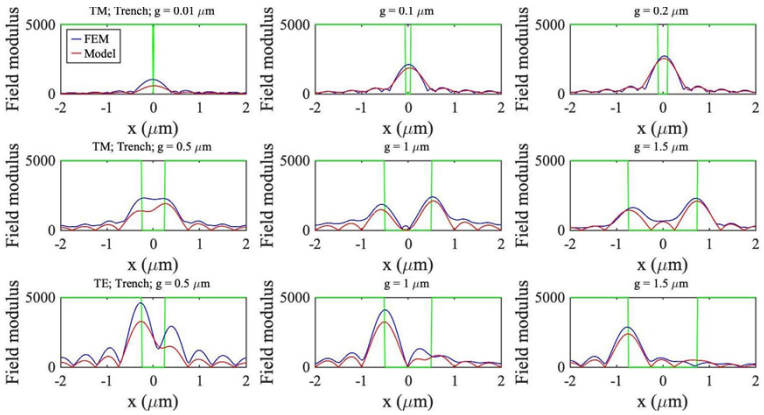


Fig. 4. Line variations of field modulus in images of trenches, for one wave incident at $\theta_0 = 50^o$. Upper – TM; lower – TE. Blue – FEM; red – GTD scattering model; green - structure.

Scattering models may easily be constructed for more complex objects and illuminations. For example, Fig. 5 compares normalized intensity images for a pair of adjacent mesas of width $w = 0.1\mu m$ and different centre-to-centre separations s, now assuming TE and TM polarizations together and double-sided incidence. Good results are again obtained for large separations. However, significant errors occur at s = 0.6 μm (corresponding to an air gap of λ) and s = 0.3 μm (close to $\lambda/2$). From the dimensions involved, these are likely due to resonance effects that are not described by the simple scattering model.

It is important to recognize that all the results in Figs. 3–5 were obtained using the coefficient values from Table 1. Despite the discrepancies noted above, the scattering models yields good approximations to the results of detailed numerical simulation over a wide range of structures and geometric parameters. For now, we therefore accept the limit to feature spacing and consider how the model may be adapted to three dimensions. The general arrangement was previously shown in Fig. 2; the main difficulty is that identification of edges and construction of scattering functions must be automated.

Optics EXPRESS

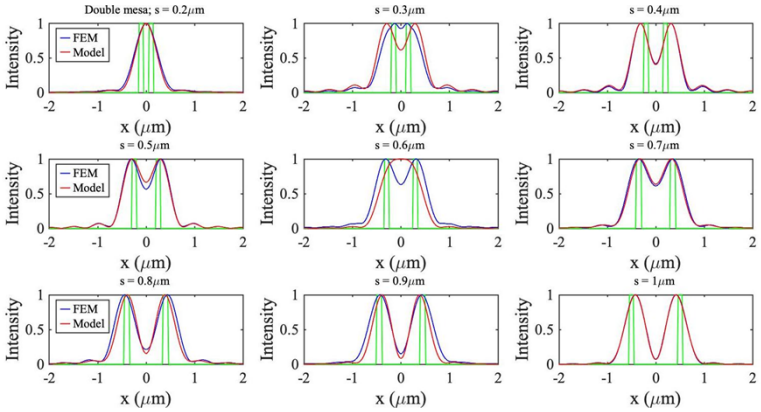


Fig. 5. Line variations of normalized intensity in images of double mesas of different separations s, for two waves at $\theta_0 = 50^o$ and $\theta_0 = -50^o$ and TE and TM polarizations together. Blue – FEM; red – GTD scattering model; green - structure.

4. Approximate 3D scattering model

We first consider scattering from an infinite line object. Figure 6(a) shows normal incidence at an angle θ_0 on an edge parallel to the y-axis, with the polarization vector (red) in the (x, y) plane. We refer to this as TE-like polarization; the perpendicular polarization is TM-like. The propagation vectors of the incident and propagating scattered waves are blue and green arrows, respectively; the latter are found by rotating the incident wave vector about the edge. Because all wave vectors lie in the (x, z) plane, some scattering must always enter the lens. Figure 6(b) shows oblique incidence, described by the additional angle ψ_0. All wave vectors now have a y-component $k_y = k_0 sin(\theta_0) sin(\psi_0)$, so the fan of scattered vectors forms a Keller cone. Less scattering can now enter the lens, and, for sufficiently large ψ_0, this will fall to zero.

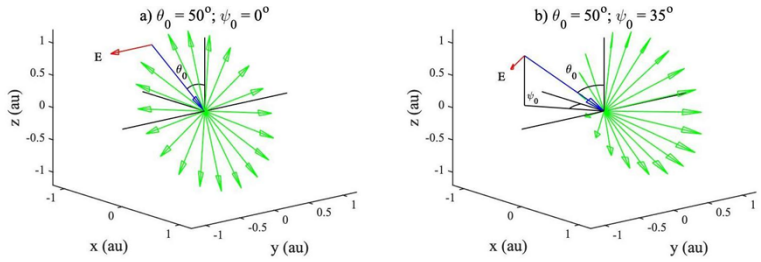


Fig. 6. Scattering from an infinite edge at a) normal and b) oblique incidence.

To quantify this effect, Fig. 7(a) shows a Fourier-domain representation of the processing performed by the lens. The pupil function P is the green circle of radius k_L, shown here for $\theta_L = 30^o$. For $\psi_0 = 0$, the transform of the object field is the thin blue line at $k_y = 0$. Only spatial frequencies with $|k_x| \leq k_L$ (thick blue line) contribute to the image, so inverse transformation yields the sinc-function variations previously obtained in 2D. For $\psi_0 \neq 0$, the transform is offset vertically by k_y; the cyan line shows the result for $\theta_0 = 50^o, \psi_0 = 35^o$. Only spatial frequencies with $|k_x| \leq \sqrt{(k_L^2 - k_y^2)}$ (thick cyan line) now contribute. Inverse transformation will again yield a sinc-function variation, but with a weaker, wider peak, whose amplitude must fall to zero at $\psi_{0M} = \sin^{-1}\{\sin(\theta_L)/\sin(\theta_0)\}$. Dark-field illumination implies that θ_0 must be greater than θ_L by a practical clearance, so this value is less than 90^o. Figure 7(b) shows variations of

Optics EXPRESS

ψ_{0M} with θ_0 for different θ_L, which imply that ψ_{0M} is very restricted for small θ_L. The most important illuminating waves then have $\psi_0 \approx 0^o,\ 90^o, 180^o$ and 270^o for Manhattan geometries, significantly reducing the number of waves needed for simulation.

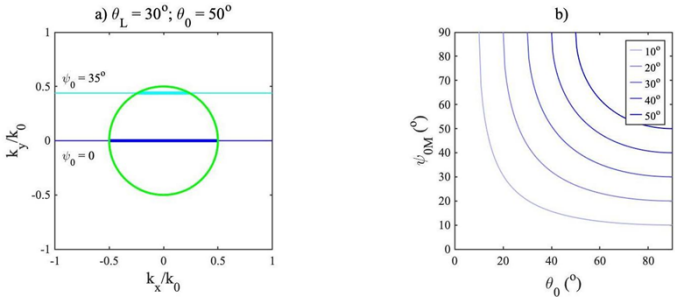


Fig. 7. a) Filtering of edge waves by the pupil; b) variation of ψ_{0M} with θ_0 for different θ_L.

A 3D model of dark-field imaging can then be constructed by assuming that:

1. Structures have 2D 'Manhattan' layouts with mesa edges parallel to the x- and y-axes. Only edge waves contribute to the image. Edges may be located by edge detection but must be separated into leading and trailing groups for each illumination.

2. Edge waves arise by scattering illuminating waves into spherical waves following the ITD. This process yields primary out-of-plane scattering directly, but re-scattering of in-plane radiation by nearby edges yields secondary scattering. For a long edge, spherical waves must sum to cylindrical waves. The spherical wave diffraction coefficients d' may be found by integration, as $d' = d/2\pi$.

3. All-round illumination may be approximated using four waves incident outside the acceptance cone of the lens. Formation of an image from the object field may be simulated by Fourier transformation, filtering by the pupil function, and inverse transformation. Diffuse illumination can be modelled by incoherently summing contributions and including both polarizations and multiple angles and wavelengths.

The algorithms needed may be discussed with reference to Fig. 8. The first step is to define the layout as a set of binary values in a 2D array. For example, the left-hand part of Fig. 8(a) shows a layout $\boldsymbol{L}$ with three rectangular features. The step is to detect the feature edges. To assign the correct illumination and diffraction coefficients, these must be separated into four groups (left- and right-facing vertical edges, and up- and down-facing horizontal edges). Vertical and horizontal edges $\boldsymbol{e_V}$ and $\boldsymbol{e_H}$ can be detected by convolution with two 1D Sobel filters, as:

$$\boldsymbol{e_V} = \begin{bmatrix} +1 & 0 & -1 \\ +2 & 0 & -2 \\ +1 & 0 & -1 \end{bmatrix} * \boldsymbol{L};\ \boldsymbol{e_H} = \begin{bmatrix} +1 & +2 & +1 \\ 0 & 0 & 0 \\ -1 & -2 & -1 \end{bmatrix} * \boldsymbol{L} \tag{8}$$

Left-facing vertical edges $\boldsymbol{e_{VL}}$ can then be extracted, for example by shifting $\boldsymbol{e_V}$ to the right by one pixel, performing a pointwise AND operation with $\boldsymbol{L}$, and shifting the result back to the left by one pixel. Right-facing vertical edges $\boldsymbol{e_{VR}}$ and up- and down-facing horizontal edges $\boldsymbol{e_{HU}}$ and $\boldsymbol{e_{HD}}$ can be extracted using similar operations, to obtain the four sets of edges shown in green, cyan, red, and magenta in the right-hand of Fig. 8(a).

Optics EXPRESS

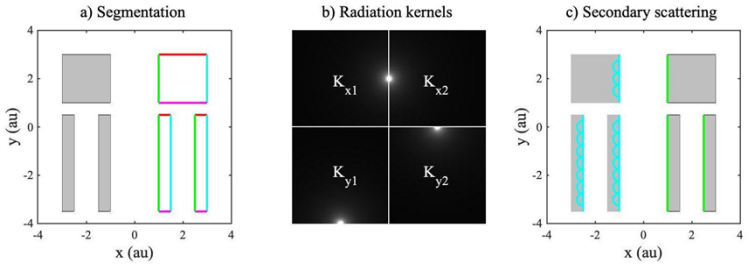


Fig. 8. a) Edge extraction, b) radiation kernels and c) secondary scattering from a vertical edge.

The third step is to illuminate the edges. Illumination patterns for each set are computed by pointwise multiplication with a complex matrix representing the appropriate wave ($\boldsymbol{E_L}$ for a left-travelling wave, and so on). For a right-facing vertical edge illuminated by a left-travelling wave (for example) we obtain $\boldsymbol{ie_{LVR}} = \boldsymbol{E_L} .* \boldsymbol{e_{VR}}$.

The fourth step is to calculate the scattering. Multiplication by the relevant diffraction coefficient (d_1' for leading edges, and d_2' for trailing edges) yields the primary out-of-plane scattering directly, for example as $\boldsymbol{PS_L} = d_1'\boldsymbol{ie_{LVR}} + d_2'\boldsymbol{ie_{LVL}}$. To compute the secondary scattering, four kernels $\boldsymbol{K_{x1}}$, $\boldsymbol{K_{x2}}$, $\boldsymbol{K_{y1}}$ $\boldsymbol{K_{y2}}$ are constructed to describe in-plane radiation from a point origin. Each kernel is a matrix with complex elements:

$$k_{ij} = \frac{\exp(-jk_o r_{ij})}{r_{ij} + r_0} \tag{9}$$

Here r_{ij} is the distance from the origin, chosen to restrict radiation to a different half-space for each kernel (to the left and right for $\boldsymbol{K_{x1}}$ and $\boldsymbol{K_{x2}}$, upwards and downwards for $\boldsymbol{K_{y1}}$ and $\boldsymbol{K_{y2}}$). The same term r_0 is again used to prevent singularities as $r_{ij} \to 0$. Figure 8(b) shows the variation of $|\boldsymbol{K}|$ for each kernel. The origin is the spot centre in each case.

Each illuminated edge pattern is then multiplied by the relevant diffraction coefficient and convolved with the appropriate kernel to generate in-plane re-radiation. For example, radiation across mesa plateaus from right-facing vertical edges illuminated by a wave travelling to the left is given by $\boldsymbol{R_{LVRM}} = d_{5A}'\boldsymbol{ie_{LVR}} * \boldsymbol{K_{x1}}$. This process attaches a radiation source to every relevant edge point; the cyan half-circles in the left-hand of Fig. 8(c) show the result. In-plane radiation is then transferred to adjacent edges (in this case, the green edges $\boldsymbol{e_{VL}}$ in the right-hand of Fig. 8(c)) by point-wise multiplication. Multiplication by the relevant diffraction coefficient then yields secondary out-of-plane scattering, e.g. as $\boldsymbol{SS_{LM}} = d_{4A}'\boldsymbol{R_{LVRM}}.*\boldsymbol{e_{VL}}$. The process must then be repeated for the secondary scattering $\boldsymbol{SS_{LA}}$ across air gaps. Primary and secondary scatterings are then summed coherently for each illuminating wave and direction to create four different scattering patterns, e.g. as $\boldsymbol{S_L} = \boldsymbol{PS_L} + \boldsymbol{SS_{LM}} + \boldsymbol{SS_{LA}}$.

Finally, a lens pupil function $\boldsymbol{P}$ is defined as a 'top-hat' low-pass filter. The scattering patterns from the four illuminating waves are then used to generate four images by FFT, pointwise multiplication with $\boldsymbol{P}$, and inverse FFT. The process is repeated for different polarizations, angles θ_0 and ψ_0 and wavelengths λ as necessary, and the component images are then summed incoherently to create the overall image. This algorithm was implemented in MATLAB, together a variety of layouts defined as binary matrices and appropriate diagnostics. Image inversion was again omitted to aid interpretation.

Optics EXPRESS

5. 3D numerical results

Results from the scattering model were benchmarked against now very lengthy 3D COMSOL simulations. Calculations were performed for PEC mesas of depth $d = 2\mu m$ surrounded by air, omitting any substrate. Figure 9 shows simulated DF intensity images of cylindrical and square prisms obtained by FEM. In each case, the feature size is $5\mu m$ and eight waves are used for illumination, with ψ_0 ranging from 0^o to 315^o in steps of 45^o . Polarization is TE and TM in upper and lower figures, respectively. In each subfigure, a combined image is shown at the lower left, and the arrows indicate contributing images. Figures 9(a), (b) and (c) show results for the cylindrical prism with $\theta_0 = 40^o, 50^o$ and 60^o. For TE polarization, each of the eight waves mainly contributes a leading-edge arc to the perimeter, which shortens as θ_0 increases. For TM polarization, the contributions are trailing-edge arcs. Similarly, Fig. 9(d) shows that the four waves at $\psi_0 \approx 0^o, 90^o, 180^o$ and 270^o contribute sides of the square prism at normal incidence, while waves at $\psi_0 \approx 45^o, 135^o, 225^o$ and 315^o provide additional vertex detail. If vertices are unimportant, four waves will be sufficient for illuminating Manhattan layouts.

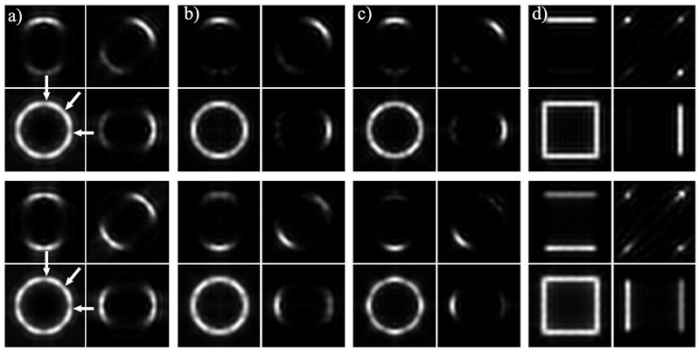


Fig. 9. Simulated images of cylindrical prism at a) $\theta_0 = 40^o$, b) 50^o and c) 60^o obtained using FEM with 8 waves incident. d) image of square prism at $\theta_0 = 50^o$. Upper: TE, lower: TM.

The four-wave model has been used to simulate many structures, simply using different layouts. For example, Figs. 10(a) and 10(b) shows the layout and extracted edges for four touching beams of width $1\mu m$. Mesa surfaces are shown in grey, horizontal edges in red and magenta, and vertical edges in green and cyan. Simulations were carried out for $\lambda = 0.5\mu m, \theta_0 = 50^o, \theta_L = 30^o, r_0 = \lambda/2$ and TE polarization. Figures 10(c) and 10(d) compares intensity images predicted by the FE and scattering models, and Figs. 10(e) and 10(f) compare scans along the green and red lines. Both models predict similar images, with a bright central ring due to re-scattering. Figure 11 shows similar results for crossed pairs of nanoscale beams of width $0.1\mu m$ and separation $1\mu m$, again for TE polarization. In each model, increased brightness is now predicted only at beam intersections. Figure 12 shows results for a generic NEMS resonator based on a small table suspended on parallel nanoscale beams (again of width $0.1\mu m$ and separation $1\mu m$) and driven by electrodes on either side, for TM polarization.

Agreement with FEM is now less good, especially for the nanoscale beams, presumably due to the coherent summation of a limited number of approximated scattering terms. However, electrode edges appear curved in each case, and it is again simple to trace this feature to in-plane scattering. Despite some line-scan variations, there is good qualitative agreement between the two model predictions in each example. Because of the all-round illumination, the differences between leading and trailing edges highlighted in Fig. 9 disappear. However, execution times are dramatically reduced for the scattering model compared with FEM, by a factor of ~1000. TE and TM results may be summed to obtain unpolarized images, and additional waves included to

Optics EXPRESS

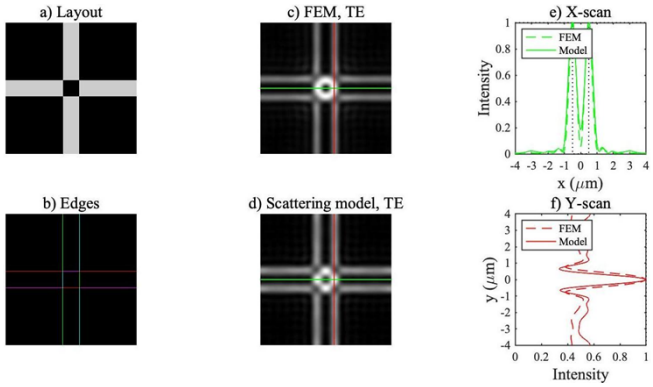


Fig. 10. a) Layout and b) edges for crossed microscale beams; c), d) images simulated using the FE and scattering models; e), f) comparative line-scans in x-and y-directions. TE.

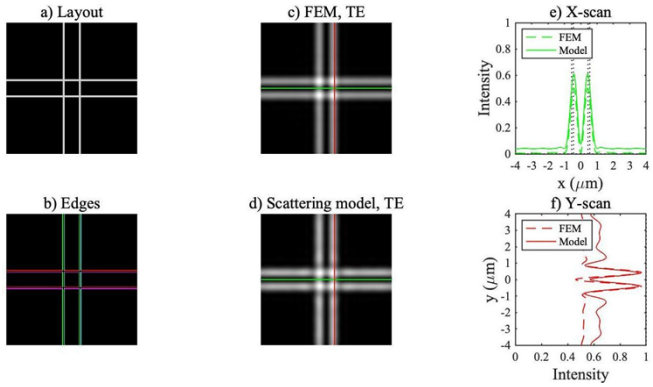


Fig. 11. a) Layout and b) edges for crossed nanoscale beams; c), d) images simulated using the FE and scattering models; e), f) comparive line-scans in x-and y-directions. TE.

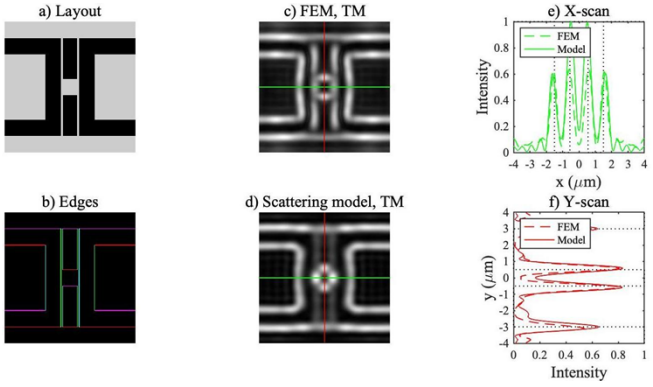


Fig. 12. a) Layout and b) edges for a NEMS resonator; c), d) comparative images simulated using the FE and scattering models; e), f) comparative line-scans in x-and y-directions. TM.

Optics EXPRESS

improve the modelling of diffuse illumination. We conclude that the scattering model may allow a reasonable and rapid prediction of expected images.

6. Conclusions

An approximate model has been developed for DF imaging of HAR structures, based on the GTD. In this regime, image formation is dominated by waves scattered and re-scattered from edges rather than from the features themselves. Computational demands have been lowered by replacing 3D calculations with 2D ones, limiting the number of illuminating waves, simplifying in-plane scattering, and approximating diffraction coefficients. Execution is automated, and all that is required is a layout array. 2D and 3D simulations both compare well with FEM results, provided feature separations are greater than around a wavelength. TE results are more accurate than TM results, due to the unimportance of in-plane radiation across mesas in the former case, but this may be unimportant for unpolarized images. Potential applications include predicting the results of low-cost optical inspection of NEMS to identify missing features.

The scattering model currently suffers from four main deficiencies. Firstly, it is restricted to Manhattan geometries; however, it should be relatively simple to allow features with edges at 45^{o} using convolution operators that operate diagonally. Secondly, as noted in Section 2, it cannot model closely spaced features, due to the limited number of scatterings included. Further work is therefore needed to consider the inclusion of higher-order terms. Thirdly, as noted in Section 5, some details are omitted at vertices, due to the limited number of illuminating waves. These could be reintroduced by increasing the number of waves, at least to eight. Finally, the model effectively assumes that features end at the edge of the calculation window. For periodic arrangements, this effect could be mitigated by a calculation window containing multiple periods. There is considerable scope to address these points.

Disclosures. The authors declare no conflicts of interest.

Data availability. Data underlying the results presented in this paper are not publicly available at this time but may be obtained from the authors upon reasonable request.

References

1. H. H. Hopkins, "On the diffraction theory of optical images," Proc. R. Soc. Lond. A **217**(1130), 408–432 (1953).
2. E. C. Kintner, "Method for the calculation of partially coherent imagery," Appl. Opt. **17**(17), 2747–2753 (1978).
3. N. Streibl, "Three-dimensional imaging by a microscope," J. Opt. Soc. Am. A **2**(2), 121–127 (1985).
4. C. J. R. Sheppard, "The optics of microscopy," J. Opt. A: Pure Appl. Opt. **9**(6), S1–S6 (2007).
5. D. Nyyssonen, "Theory of optical edge detection and imaging of thick layers," J. Opt. Soc. Am. **72**(10), 1425–1436 (1982).
6. J. T. Sheridan and C. J. R. Sheppard, "Coherent imaging of periodic thick fine isolated structures," J. Opt. Soc. Am. A **10**(4), 614–632 (1993).
7. J. T. Sheridan and C. J. R. Sheppard, "Modelling of images of square-wave gratings and isolated edges using rigorous diffraction theory," Opt. Comm. **105**(5-6), 367–378 (1994).
8. C. M. Yuan and A. J. Strojwas, "Modeling optical microscope images of integrated-circuit structures," J. Opt. Soc. Am. A **8**(5), 778–790 (1991).
9. T. Tamir, H. C. Wang, and A. A. Oliner, "Wave propagation in sinusoidally stratified dielectric media," IEEE Trans. Microwave Theory Techn. **12**(3), 323–335 (1964).
10. C. B. Burckhardt, "Diffraction of a plane wave at a sinusoidally stratified dielectric grating," J. Opt. Soc. Am. **56**(11), 1502–1509 (1966).
11. M. G. Moharam and T. K. Gaylord, "Diffraction analysis of dielectric surface-relief gratings," J. Opt. Soc. Am. **72**(10), 1385 (1982).
12. M. G. Moharam and T. K. Gaylord, "Three-dimensional vector coupled wave analysis of planar-grating diffraction," J. Opt. Soc. Am. **73**(9), 1105–1112 (1983).
13. M. Totzek, "Numerical simulation of high-NA quantitative polarization microscopy and corresponding near-fields," Optik **112**(9), 399–406 (2001).
14. J. Qin, R. M. Silver, B. M. Barnes, *et al.*, "Deep subwavelength nanometric image reconstruction using Fourier domain optical normalization,," Light: Sci. Apps. **5**(2), e16038 (2016).
15. G. L. Wojcik, D. K. Vaughan, and L. K. Galbraith, "Calculation of light scatter from structures on silicon surfaces," Proc. SPIE **0774**, 21–32 (1987).

Optics EXPRESS

16. T. Pahl, S. Hegermeier, M. Künne, *et al.*, "3D modeling of coherence scanning interferometry on 2D surfaces using FEM," Opt. Express **28**(26), 39807–39826 (2020).
17. J. Krüger, R. Köning, and B. Bodermann, "Systematic approach on illustrating the challenges represented by optical bidirectional measurements using rigorous simulations," Proc. SPIE **11057**, 9 (2019).
18. T. Pahl, S. Hegermeier, J. Bischoff, *et al.*, "Rigorous 3D modelling of confocal microscopy on 2D surface topographies," Meas. Sci. Technol. **32**(9), 094010 (2021).
19. R. Capoglu, J. D. Rogers, A. Taflove, *et al.*, "The microscope in a computer: image synthesis from three-dimensional full-vector solutions of Maxwell's equations at the nanometer scale," Prog. Opt. **57**, 1–91 (2012).
20. R. Guerrieri, T. K. Tadros, J. Gamelin, *et al.*, "Massively parallel algorithms for scattering in optical lithography," IEEE Trans. Comput.-Aided Des. Integr. Circuits Syst. **10**(9), 1091–1100 (1991).
21. I. R. Capoglu, C. A. White, J. D. Rogers, *et al.*, "Numerical simulation of partially-coherent broadband optical imaging using the FDTD method," Opt. Lett. **36**(9), 1596–1598 (2011).
22. K. D. Lucas, H. Tanabe, and A. J. Strojwas, "Efficient and rigorous three-dimensional model for optical lithography simulation," J. Opt. Soc. Am. A **13**(11), 2187–2199 (1996).
23. E. Marx, "Images of strips on and trenches in substrates," Appl. Opt. **46**(23), 5571–5587 (2007).
24. A. J. W. Sommerfeld, "Mathematische theorie der diffraction," Math. Ann. **47**(2-3), 317–374 (1896).
25. J. B. Keller, "Geometrical theory of diffraction," J. Opt. Soc. Am. **52**(2), 116–130 (1962).
26. P. Ya. Ufimtsev, "Method of edge waves in the physical theory of diffraction," translated by U.S. Air Force Foreign Technology Division, Wright-Patterson AFB, OH, Sept. (1971).
27. R. M. Lewis and J. Boersma, "Uniform asymptotic theory of edge diffraction," J. Math. Phys. **10**(12), 2291–2305 (1969).
28. G. D. Durgin, "The practical behavior of various edge diffraction formulas," IEEE Antennas Propag. Mag. **51**(3), 24–35 (2009).
29. S. N. Karp and A. Russek, "Diffraction by a wide slit," J. Appl. Phys. **27**(8), 886–894 (1956).
30. J. B. Keller, "Diffraction by an aperture," J. Appl. Phys. **28**(4), 426–444 (1957).
31. A. Elsherbini and M. Hamid, "Diffraction by a wide double wedge," IEEE Trans. Antennas Propagat. **32**(11), 1262–1265 (1984).
32. R. Tiberio, G. Manara, G. Pelosi, *et al.*, "High-frequency electromagnetic scattering of plane waves from double wedges," IEEE Trans. Antennas Propagat. **37**(9), 1172–1180 (1989).
33. F. Capolino, M. Albani, S. Maci, *et al.*, "Double diffraction at a pair of coplanar skew edges," IEEE Trans. Antennas Propag. **45**(8), 1219–1226 (1997).
34. G. Carluccio and M. Albani, "An efficient ray tracing algorithm for multiple straight edge diffraction," IEEE Trans. Antennas Propag. **56**(11), 3534–3542 (2008).
35. K. M. Mitzner, "Incremental length diffraction coefficients," Northrop Corp. Aircraft Division Technical Report AFAL-TR-73-296 (1974).
36. G. Pelosi, S. Maci, and R. Tiberio, "Incremental length diffraction coefficients for an impedance wedge," IEEE Trans. Antennas Propag. **40**(10), 1201–1210 (1992).
37. R. Tiberio and S. Maci, "An incremental theory of diffraction: scalar formulation," IEEE Trans. Antennas Propagat. **42**(5), 600–612 (1994).
38. A. Michaeli, "Incremental diffraction coefficients for the extended physical theory of diffraction," IEEE Trans. Antennas Propagat. **43**(7), 732–734 (1995).
39. A. Khoh, G. S. Samudra, Y. Wu, *et al.*, "Image formation by use of the geometrical theory of diffraction," J. Opt. Soc. Am. A **21**(6), 959–967 (2004).
40. J. Tirapu-Azpiroz and E. Yablonivitch, "Incorporating mask topography edge diffraction in photolithography simulations," J. Opt. Soc. Am. A **23**(4), 821–828 (2006).
41. V. Farys, P. Sciavone, F. Polack, *et al.*, "Highly sensitive detection technique of buried defects in extreme ultraviolet masks using at-wavelength scanning dark field microscopy," Appl. Phys. Lett **87**(2), 024102 (2005).
42. T. Eriksson, S. Yamada, P. Venkatesh, *et al.*, "High volume nanoimprint lithography on III/V substrates: imprint fidelity and stamp lifetime," Microelectron. Eng. **88**(3), 293–299 (2011).
43. D.-M. Shyi and Y.-S. Ku, "Measurement of through silicon via etch profile by dark-field optical microscope," Proc. SPIE **8324**, 832414 (2012).
44. G. Nitzsche, R. Hild, U. Altenburger, *et al.*, "Optical image processing - a useful tool in wafer inspection," Microelectr. Engng. **23**(1-4), 391–394 (1994).
45. O. Varela Pedreira, T. Lauwagie, J. De Coster, *et al.*, "High throughput measurement techniques for wafer level yield inspection of MEMS devices," Proc. SPIE **7155**, 71550M (2008).
46. G. Ehret, "Quantitative linewidth measurement down to 100 nm by means of optical dark-field microscopy and rigorous model-based evaluation," Meas. Sci. Technol. **18**(2), 430–438 (2007).
47. R. R. A. Syms, A. Bouchaala, O. Sydoruk, *et al.*, "Optical imaging and image analysis for high aspect ratio NEMS," J. Micromech. Microeng. **29**(1), 015003 (2019).
48. R. R. A. Syms, A. Bouchaala, and O. Sydoruk, "Improved optical imaging of high aspect ratio NEMS using dark-field microscopy," Nanotechnol. **30**(28), 285301 (2019).

155.199.18.117 2023-04-14 06:16:1